Carcinogenesis vol.35 no.9 pp.1920–1930, 2014
doi:10.1093/carcin/bgu033
Advance Access publication February 6, 2014

Functional links between Snail-1 and Cx43 account for the recruitment of Cx43-positive cells into the invasive front of prostate cancer

Damian Ryszawy, Michał Sarna[1], Monika Rak, Katarzyna Szpak, Sylwia Kędracka-Krok[2], Marta Michalik, Maciej Siedlar[3], Ewa Zuba-Surma, Kvetoslava Burda[1], Włodzimierz Korohoda, Zbigniew Madeja and Jarosław Czyż*

Department of Cell Biology, Faculty of Biophysics, Biochemistry and Biotechnology, Jagiellonian University, ul. Gronostajowa 7, 30–387 Kraków, Poland, [1]Department of Medical Physics and Biophysics, AGH University of Science and Technology, 30–059 Kraków, Poland, [2]Department of Physical Biochemistry, Faculty of Biophysics, Biochemistry and Biotechnology, Jagiellonian University, ul. Gronostajowa 7, 30–387 Kraków, Poland and [3]Department of Clinical Immunology, Polish-American Institute of Pediatrics, Jagiellonian University Medical College, 30–663 Kraków, Poland

*To whom correspondence should be addressed. Tel: +48 12 6646146; Fax: +48 12 6646902;
Email: jarek.czyz@uj.edu.pl

Suppressive function of connexin(Cx)43 in carcinogenesis was recently contested by reports that showed a multifaceted function of Cx43 in cancer progression. These studies did not attempt to model the dynamics of intratumoral heterogeneity involved in the metastatic cascade. An unorthodox look at the phenotypic heterogeneity of prostate cancer cells *in vitro* enabled us to identify links between Cx43 functions and Snail-1-regulated functional speciation of invasive cells. Incomplete Snail-1-dependent phenotypic shifts accounted for the formation of phenotypically stable subclones of AT-2 cells. These subclones showed diverse predilection for invasive behavior. High Snail-1 and Cx43 levels accompanied high motility and nanomechanical elasticity of the fibroblastoid AT-2_Fi2 subclone, which determined its considerable invasiveness. Transforming growth factor-β and ectopic Snail-1 overexpression induced invasiveness and Cx43 expression in epithelioid AT-2 subclones and DU-145 cells. Functional links between Snail-1 function and Cx43 expression were confirmed by Cx43 downregulation and phenotypic shifts in AT-2_Fi2, DU-145 and MAT-LyLu cells upon Snail-1 silencing. Corresponding morphological changes and Snail-1 downregulation were seen upon Cx43 silencing in AT-2_Fi2 cells. This indicates that feedback loops between both proteins regulate cell invasive behavior. We demonstrate that Cx43 may differentially predispose prostate cancer cells for invasion in a coupling-dependent and coupling-independent manner. When extrapolated to *in vivo* conditions, these data show the complexity of Cx43 functions during the metastatic cascade of prostate cancer. They may explain how Cx43 confers a selective advantage during cooperative invasion of clonally evolving, invasive prostate cancer cell subpopulations.

Introduction

Solid tumors are maintained by the exchange of signals between phenotypically plastic cancer cells and their local microenvironment (1). Intercellular communication networks determine the homeostasis of functionally discrete tumor compartments and provide cues for cancer expansion and metastasis (2). Extrinsic stimuli transmitted by aberrant intratumoral communication systems govern a set of 'secular', proinvasive cell properties, such as momentary chemotactic motility and nanomechanical elasticity (3). Such stimuli also trigger heritable, epigenetic switches in 'metastable' cells, which, in combination with spontaneous mutations, may preserve their invasive behavior (4). They govern permanent cell predilection to colonize distant organs and are responsible for the clonal evolution of metastasis-initiating cell subpopulations (5). The symptoms of these switches include changes in locomotion strategy, in the expression of transmitters for microenviromental signals and in the functional status of gap junctional channels (6–8).

Gap junctional channels are constituted by proteins of the connexin (Cx) family. Their basic function is to mediate the intercellular exchange of small (<1 kDa) molecules in the process of gap junctional intercellular coupling (GJIC). Downregulation of tissue-specific connexin expression and GJIC deficiency were found in a number of cancerous tissues. However, the paradigm of cancer-suppressive connexin function has been challenged by recent studies that have suggested a stage-specific connexin function during cancer development (6,9). Accordingly, connexin deficiency may exert selective pressure on clonally expanding cells during early stages of carcinogenesis, whereas the reexpression of connexins in certain primary tumor compartments accompanies the formation of the cancer 'invasive front'. Cx43 expression enhances the motility and invasion of cancer cells in a GJIC-dependent and GJIC-independent manner (10–14). These observations may explain why connexin-expressing cancer cells are often abundant in secondary tumors (15,16). However, the links between Cx43 function and clonal evolution of metastasis-initiating cells have not yet been experimentally addressed. For instance, the role of Cx43 in prostate cancer progression has been illustrated by a correlation between intrinsic Cx43 expression and prostate cancer cell tumorigenic potential *in vivo* and invasive properties *in vitro*. Prostate cancer cells with increased Cx43 expression displayed increased ability to form metastasis in bones (17–19). Attempts to elucidate the dynamics of possible functional links between Cx43 expression and clonal evolution of prostate cancer cells might thus be helpful in evaluating predictive metastatic potential of prostate cancers (20). Prompted by these insights, we hypothesized that Cx43 expression and prostate cancer cell invasive behavior are concomitantly regulated during the functional speciation of invasive cancer cells.

In particular, the sequential events of epithelial–mesenchymal transition (EMT), such as the acquisition of rear-front cell polarity and increase of cell motility and elasticity, participate in the prostate cancer metastatic cascade together with the reverse process of mesenchymal–epithelial transition (21,22). Stochastic fluctuations of transcriptional regulators, including Snail-1, and/or extrinsic stimuli may trigger both processes and induce permanent cell reprogramming (23,24). Notably, connexins and connexons interact with a myriad of submembrane protein assemblies within the gap junction proteome (25). These interactions open a range of possibilities for GJIC-independent involvement of Cx43 in colonization of distant organs by clonally evolving cancer cells. Thus, it was of interest to check whether Cx43 could directly participate in EMT-related phenotypic shifts of prostate cancer cells toward an invasive phenotype.

The pattern of prostate carcinogenesis is determined by cellular metastable states biased toward cell expansion and/or "transdifferentiation" and predefined by phenotypic plasticity and epigenetic memory of cancer cells (23,26). Prompted by previous reports on this topic (27–30), we presumed that the events involved in the heterogeneity of prostate cancer AT-2 cells *in vitro* recapitulated the functional speciation processes within primary tumor compartments *in vivo* (31). We used this model as a tool to follow the links between EMT-related phenotypic shifts and Cx43 expression and to delineate the mechanisms of Cx43 involvement in the regulation of prostate cancer cell invasive potential.

Abbreviations: AFM, atomic force microscope; EMT, epithelial–mesenchymal transition; EPI, endothelial penetration index; FA, formaldehyde; FBS, fetal bovine serum; FRET, fluoerescence resonance energy transfer; GJIC, gap junctional intercellular coupling; IgG, immunoglobin G; IMC, interference modulation contrast; SEM, standard error of the mean; siRNA, small interfering RNA; TEI, transendothelial migration index; TGF, transforming growth factor.

Materials and methods

Cell cultures

AT-2 and MAT-LyLu cells were grown in fetal bovine serum (FBS)-supplemented RPMI 1640 (Lonza, Basel, Switzerland). DU-145 and PNT-2 cells were cultured in FBS-supplemented DMEM-F12 Ham's medium (Sigma, St. Louis, MO) (17,18). Human microvascular endothelial cells (HMEC-1) were cultured in MCDB 131 medium (Gibco BRL, Life Technologies, Grand Island, NY) supplemented with 10% FBS, 1 µg/ml hydrocortisone, 10 ng/ml epidermal growth factor and 2 mM L-glutamate (all from Sigma). Invasive AT-2 subsets were propagated from cells seeded on the upper side of transwell inserts (pore diameter: 8 µm; Corning, NY) in 24-well plates (Becton-Dickinson, Franklin Lakes, NJ) at a density of 300 cells/mm^2, which managed to transmigrate microporous membranes during the first 48 h (AT-2_48) and between 48 and 72 h after seeding (AT-2_72) (18). AT-2 subclones were established from cells seeded at clonal density (5 cells/cm^2) into 60-mm Petri dishes. Five days later, individual clones were discriminated by morphology, mechanically dissected by micropipette and transferred to multiwell plates (Becton-Dickinson) for further propagation. The established subsets and subclones were cultivated in standard medium for ca. 15 generation times (five passages at 1:8). Cell proliferation analyses were performed with a Coulter Z2 Counter (Beckman Coulter, Fullerton, CA) and doubling times were calculated from the growth curves according to the formula: doubling times = $T\ln 2/\ln(X_e/X_b)$, where: T is the incubation time; X_b and X_e are the cell numbers at the beginning and at the end of the incubation time, respectively. Where indicated, the culture medium was supplemented with transforming growth factor (TGF)-β (No. 356041, BD Bioscience, 10 ng/ml) and 18-alpha-glycyrrhetinic acid (50 µM, No. G8503, Sigma).

Immunolabeling

Localization of Cx43, Snail-1 and p-Smad2 (Ser467) and the cytoskeleton architecture were analyzed in formaldehyde (3.7%)-fixed, Triton X-100 (0.1%) permeabilized cells. Where indicated, the cells were fixed in suspension or with methanol:acetone (7:3, −20°C) as described previously (17,32). The following primary antibodies were used: mouse anti-vimentin immunoglobin G (IgG; No. V5255, Sigma), mouse anti-Cx43 IgM (No. C8093. Sigma), rabbit anti-Snail-1 IgG (No. AV33314, Sigma), mouse anti-N-cadherin IgG (No. C3865, Sigma), rabbit anti-Cx43 IgG (No. C6219, Sigma), rabbit anti-vinculin IgG (No. V9131, Sigma), and mouse anti-pSmad2 IgG (No. SAB4300251, Sigma). The cells were labeled with the following: Alexa 488-conjugated goat anti-mouse IgG (No. A11001, Invitrogen, Carlsbad, CA), Alexa 546-conjugated goat anti-mouse IgM (No. No. A21045, Invitrogen), Alexa 488-conjugated goat anti-rabbit IgG (A11008, Invitrogen), APC-conjugated goat anti-mouse IgM (No. 406509, BioLegend, San Diego, CA), PE-conjugated goat anti-mouse IgG (No. 405307, BioLegend). Where indicated, the cells were counterstained with TRITC-conjugated phalloidin (No. 77418, Sigma) and Hoechst 33258 (No. B2883, Sigma) or 7AAD (No 51-2359KC, BD Pharminogen).

Fluorescence microscopy and imaging cytometry

Image acquisition was performed with a Leica DMI6000B microscope (DMI7000 version; Leica Microsystems, Wetzlar, Germany) equipped with the total internal reflection fluorescence, Nomarski interference contrast and interference modulation contrast modules. LAS-AF deconvolution software was used for image processing. Fluoerescence resonance energy transfer (FRET) experiments were performed with a Leica DMI6000B system equipped with external filter wheel CFP/YFP (cyan fluorescent protein/yellow fluorescent protein) FRET set (11522073) controlled by FRET SE Wizard software (Leica). Images were registered with ×100, NA-1.47 oil immersion objective in 37°C/5% CO_2 using 14-bit Hamamatsu 9100–02 EM-CCD camera controlled by the Leica Application Suite Advanced Fluorescence software. Two-channel-corrected FRET efficiency [FRET SE (sensitized emission)] was calculated based on the following formula: $(B - A\beta - C\gamma)/C$, where A, B, C correspond to the intensities of donor, FRET and acceptor signals, whereas β and γ are the calibration factors generated by acceptor only and donor only references. Imaging cytometry of the cells fixed and immunostained in suspension was performed with a FlowSight® imaging cytometer (Amnis Corp., Seattle, WA; for details see legend to Supplementary Figure S2, available at *Carcinogenesis* Online).

Coimmunoprecipitation, immunoblotting and tandem mass spectrometry

Cells were dissolved in a lysis buffer and samples containing 30 µg of protein were either directly separated by 15% sodium dodecyl sulfate–polyacrylamide gel electrophoresis or subjected to coimmunoprecipitation with rabbit polyclonal anti-Cx43 IgG (Sigma) (18,33). Crude proteins and immune complexes were transferred into polyvinylidene difluoride membranes (Hybond-P, Amersham Pharmacia Biotech, UK). The membranes were then incubated with a primary antibody: rabbit polyclonal anti-Cx43 or anti-Snail-1 IgG; mouse polyclonal anti-pan-cytokeratin (No. C2562, Sigma), anti-Slug (WH0006591M5, Sigma) and anti-Twist1 (T6451, Sigma) IgG or monoclonal anti-N-cadherin, anti-vimentin (No. V5255, Sigma) and anti-α-tubulin IgG (No. T9026, Sigma). The detection of antibodies was done using the relevant HRP-conjugated secondary antibodies (goat anti-mouse IgG and goat anti-rabbit IgG; No. G21040 and G21234, respectively, Invitrogen), Super Signal West Pico Substrate (Pierce, Rockford, IL) and the MicroChemii imaging system (SNR Bio-Imaging Systems, Jerusalem, Israel). Concomitantly, liquid chromatography and tandem mass spectrometry was performed as described in ref. (34) with the reversed-phase liquid chromatography (RP-LC) system (UltiMate 3000RS LCnanoSystem, Dionex) coupled to a quadrupole time-of-flight mass spectrometer (micrOTOF-Q II, Bruker Daltonics, Bremen, Germany).

Time-lapse videomicroscopy

Cell movement was recorded with a Leica DMI6000B time-lapse system equipped with a temperature/CO_2 chamber, interference modulation contrast optics and a cooled, digital DFC360FX CCD camera. The cell trajectories were constructed from a sequence of cell centroid positions recorded at 300 s time intervals using a dry ×20, NA-0.75 objective. Total length of cell trajectory (µm), velocity of cell movement (speed; total length of cell trajectory/time of recording; µm/min) and total length of cell displacement (i.e. the distance from the starting point directly to the cell's final position; µm) were quantified with the Hiro program (written by W. Czapla) as described in ref. (32).

Atomic force microscopy

Nanomechanical studies were performed using the Agilent 5500 atomic force microscope (Agilent Technologies, Santa Clara, CA), in 37°C as described previously (35). The values of Young's modulus were estimated according to the Hertz model. Force-displacement curves were collected using sharpened silicon nitride cantilevers (Veeco Probes, New York; tip radius of <50 nm). The half opening angle of the atomic force microscope tip was 25° and the Poisson ratio of the cell was taken to be 0.5, the value typical for soft biological materials. The measurements were collected in the force ranges resulting in shallow indentations of the cells (<500 nm). Curves from 10 to 20 randomly selected points were chosen for each cell and 10 force curves were measured at each point for statistical analysis. At least 15 cells were investigated for each population.

Gap junctional intercellular coupling

Calcein-loaded (No. C3100MP, Invitrogen) donor cells were plated on monolayers of acceptor cells grown on coverslips in Petri dishes at the ratio of 1:50 as described in ref. (36) and intercellular calcein transfer was evaluated using a Leica DMI6000B microscope in the epifluorescence mode. Coupling index (C_i) was quantified as the percentage of donor cells coupled with at least one acceptor cell.

Transmigration tests

HMEC-1 cells were seeded on the upper side of transwell inserts in 24-well plates at 2 × 10^4 cells/well and grown to confluence for 72 h. Thereafter, 2 × 10^3 AT-2 cells were seeded at the top of the filter, allowed to transmigrate in chemodynamic conditions for 24 h, before the insert was transferred to another well for the next 24 h. This step was repeated 5 times. The initial cell numbers in the wells were determined as a function of population doubling time and time of cultivation and expressed as the percentage of the seeded cells [transendothelial migration index (TEI)]. A corresponding protocol was used to elucidate AT-2 transmigration through uncovered membranes (transmembrane migration index). For estimation of the endothelial penetration index (EPI), AT-2 cells were seeded on a HMEC-1 monolayer on coverslips and incubated for 6 h before F-actin/DNA staining and microscopic estimation of the percentage of AT-2 cells capable of disrupting the endothelial continuum.

Cell transfection

Cells were cultured in the antibiotic-free medium supplemented with 10% FBS. After 24 h, cells were treated with complexes of 1.5 µl Lipofectamine™ 2000 Reagent (11668-019, Invitrogen) and 1 µg plasmid DNA/small interfering RNA (siRNA) in Opti-MEM® I Reduced Serum Medium (31985070, Gibco-Life Technologies) according to the manufacturer's protocol. In cotransfection experiments, 0.5 µg of each plasmid (1 µg in total) was used. After 24 h the medium was replaced with standard medium supplemented with 10% FBS and antibiotics. The efficiency of silencing was analyzed with immunoblotting. The following siRNA/plasmids were used: MISSION® esiRNA GJA1 (EHU105621, Sigma), SNAI-1 siRNA and siRNA-A (sc-38398 and sc-37007, Santa Cruz Biotechnology, Dallas, TX), pmTurquoise2-α-Tubulin (#36202, Addgene), pTRE-TIGHT-Cx43-eYFP (#31807, Addgene; FRET), Snail_pGL2 (#31694, Addgene) and pcDNA 3.1 (V790-20, Invitrogen) (37–39).

Results

Snail-1^{bright}/Cx43^{bright} subpopulation of AT-2 cells displays a high invasive potential

The clusters of tightly attached epithelioid cells were accompanied by dispersed microclones of rear/front polarized cells in routinely propagated AT-2 populations. An EMT marker, vimentin, was seen in AT-2 cells, regardless of their phenotype, whereas fibroblastoid (dispersed) clusters of AT-2 cells displayed elevated Cx43 and Snail-1 protein levels (Figure 1A). At the single cell level, discrete Snail-1^{bright}/Cx43^{bright} (3.48%) and Snail-1^{bright}/N-cadherin^{bright} AT-2 subpopulations (3.76%; Figure 1B) could be discriminated by imaging cytometry.

The correlation between Cx43 and Snail-1 expression levels suggested functional links between EMT-related phenotype and Cx43 function in AT-2 cells. Therefore, we further propagated AT-2 subsets as the progenies of the cells that showed a tendency to penetrate microporous membranes in chemodynamic conditions. In comparison with the native AT-2 population, the 'invasive' AT-2_48 subset was enriched in fibroblastoid cells (Figure 1C). AT-2_48 cells had much higher motility (Figure 1C) and elasticity (Figure 1D) than native AT-2 cells. This was reflected in the narrow distribution of Young's modulus (E) values estimated with atomic force microscope for AT-2_48 cells, with a local maximum at 2.5 kPa. AT-2_72 cells originated from AT-2 cells, which followed the first wave of transmigration. They had a more diversified morphology than AT-2_48 cells (Figure 1C). Motile activity (Figure 1C) and elasticity of AT-2_72 cells (Figure 1D) were lower than those of AT-2_48 cells. The AT-2_72 subset was only slightly enriched in elastic cells, whereas an almost equal E

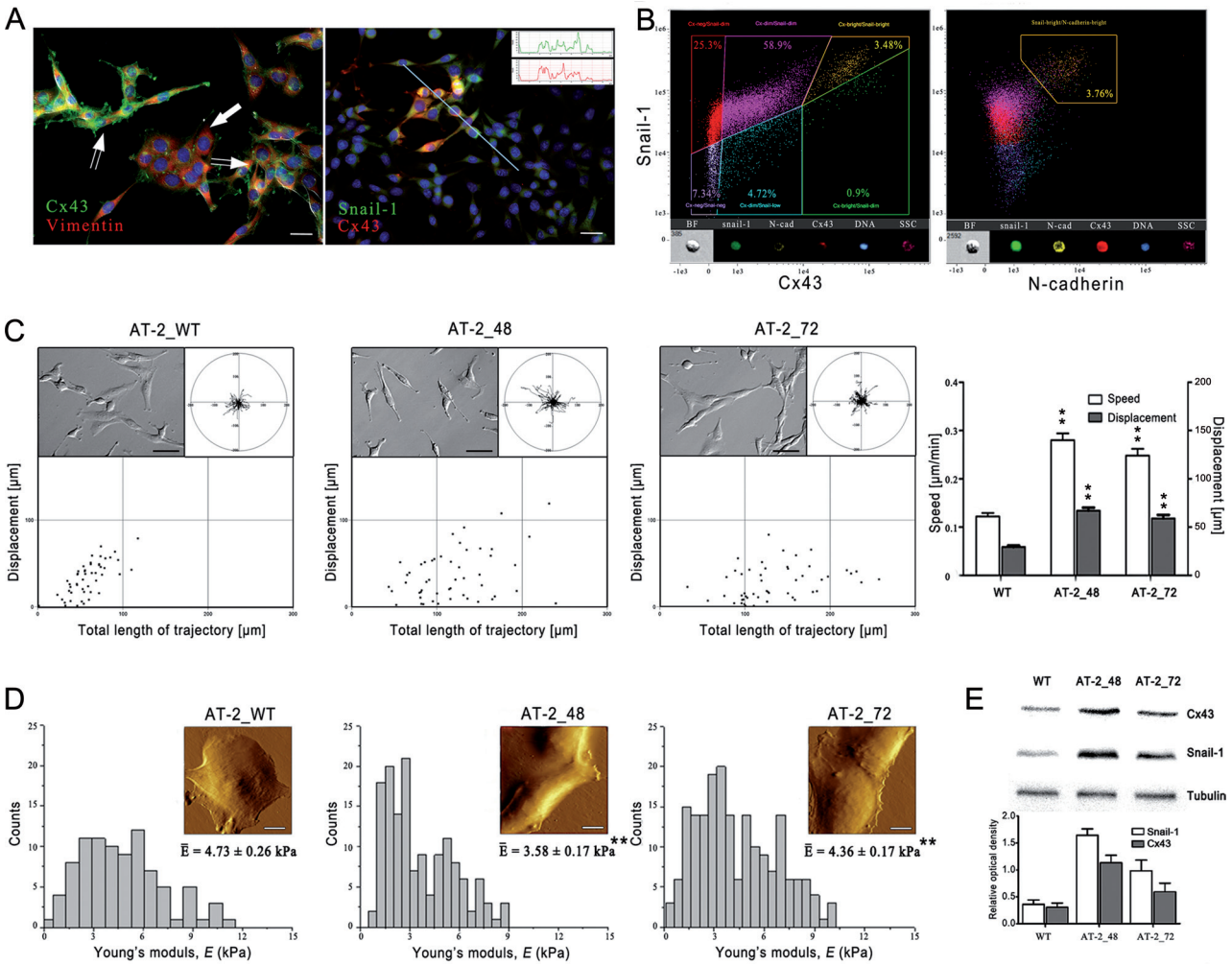

Fig. 1. Phenotypic heterogeneity of AT-2 cells. (**A**) AT-2 cells were seeded at the density of 5×10^2 cells/cm^2 and allowed to form clones (epithelioid—single arrow and fibroblastoid—double arrows) for 72 h. Cells were fixed/permeabilized with formaldehyde (FA)/Triton X-100 and immunostained against vimentin and Cx43 (left panel) and Cx43 and Snail-1 (right panel). Histograms show the colocalization of immunofluorescence signals along the indicated scan line. Scale bar: 25 µm. (**B**) AT-2 cells were fixed/permeabilized with FA/Triton X-100 in suspension, stained against Cx43, Snail-1 and N-cadherin and analyzed with imaging cytometry (see Supplementary Figure S2, available at *Carcinogenesis* Online). Compensated dot-plots comprise 50 000 events, classified based on their bright field ratios and nuclear contrast. Inserts depict images of a representative event in relevant channels. (**C**) Native AT-2 (WT) cells and invasive AT-2 subsets were seeded at the density of 2×10^4 cells/cm^2 and their morphology and motility was visualized by interference modulation contrast (IMC) and time-lapse videomicroscopy, respectively, after 24 h. Dot-plots and column chart show movement parameters at the single cell and population level, respectively. Cell trajectories are depicted as circular diagrams (axis scale in micrometer) drawn with the initial point of each trajectory placed at the origin of the plot (registered for 8 h; $N > 50$). Statistical significance was performed with the non-parametric Mann–Whitney test (**$P \leq 0.01$). Error bars represent standard error of the mean (SEM). Inserts depict cell morphology depicted by IMC. Scale bar: 50 µm. (**D**) AT-2 populations were seeded at the density of 2×10^2 cells/cm^2 and their nanomechanical elasticity probed with atomic force microscope (AFM) as described in Materials and methods. Young's modulus (E) is given in kilopascals (kPa). Examples of scan areas are depicted in inserts. Scale bar: 10 µm. Data in inserts are expressed as means ± SD and analyzed with two-sample-independent Student's *t*-test; **$P \leq 0.01$. (**E**) Immunoblot analyses of Snail-1 and Cx43 expression levels in native AT-2 cells and invasive AT-2 subsets. Relative band intensities were calculated relative to the corresponding control (α-tubulin) using the ImageJ gel analysis tool. All results are representative of three independent experiments.

distribution (between 2.0 and 6.0 kPa) was observed for native AT-2 cells. Relatively high Cx43 and Snail-1 expression levels in AT-2_48 and AT-2_72 cells (Figure 1E) indicated that Snail-1^{bright}/Cx43^{bright} cells were predominantly recruited to the AT-2 invasive front under conditions that imitated early invasive stages of prostate cancer.

Incomplete EMT-related phenotypic transitions account for AT-2 heterogeneity

For an in-depth examination of the hallmarks of AT-2 heterogeneity, we further isolated a number of morphologically distinct AT-2 subclones. Epithelioid AT-2_Ep1 and AT-2_Ep2 cells exhibited an actin cytoskeleton organized in cortical rings accompanied by microfilament bundles attached to focal adhesions (Figure 2A). In contrast, F-actin was concentrated in small protrusions of epithelioid AT-2_Ep3 and fibroblastoid AT-2_Fi1, AT-2_Fi2 and AT-2_Fi3 cells. Phenotypic stability of AT-2 subclones maintained over multiple cell divisions was paralleled by differences in their proliferation rates (Figure 2B), elasticity modules and cell motility. Fibroblastoid AT-2_Fi2 cells were less elastic than other fibroblastoid subclones (Figure 2C, see Supplementary Figure S1A, available at *Carcinogenesis* Online) but displayed the highest motile activity among fibroblastoid and epithelioid AT-2 subclones (Figure 2D, see Supplementary Figure S1B, available at *Carcinogenesis* Online). At the expression level, however, no straightforward correlation was observed between cell phenotype and the expression of vimentin and cytokeratin. Contrary to E-cadherin, which was absent in all AT-2 subclones, N-cadherin was present and was more intensely expressed in fibroblastoid subclones. In contrast to Twist and Slug, considerable Snail-1 expression correlated with fibroblastoid morphology of AT-2 subclones and elevated levels of Cx43 in AT-2_Ep3, AT-2_Fi2 and AT-2_Fi3 cells, but the highest expression of both proteins was observed in AT-2_Fi2 cells (Figure 2E). Conceivably, subtle differences in the proportions of Snail-1^{bright}/Cx43^{dim} and Snail-1^{bright}/Cx43^{bright} cells (Supplementary Figure S2, available at *Carcinogenesis* Online) account for the heterogeneity of AT-2 subclones with regard to Snail-1/Cx43 expression pattern.

Cx43 facilitates transendothelial invasion of AT-2 subclones in a GJIC-dependent manner

To estimate the link between the Snail-1/Cx43 expression pattern and the invasiveness of AT-2 subclones, we further determined the efficiency of their chemokinetic transmigration. AT-2_Fi2 cells displayed the highest efficiency of transmigration through uncovered microporous membranes (transmembrane migration index; Figure 3A) and through membranes covered with endothelial continuum (TEI, Figure 3B). High TEI values estimated for AT-2_Fi2 cells correlated with their endothelial coupling index (C_i; Figure 3C). This conformed with abundant subpopulations of detergent-insoluble Cx43-rich cells (Supplementary Figure S2, available at *Carcinogenesis* Online), plasmalemmal localization of Cx43 (Figure 3D) and the high endothelial continuum penetration index of AT-2_Fi2 cells (EPI; Figure 3E, see also Supplementary Figure S3, available at *Carcinogenesis* Online; summarized in Figure 3F). Moreover, AT-2_Fi1 cells displayed low TEI and C_i, whereas administration of 18-alpha-glycyrrhetinic acid (50 μM) evoked the attenuation of AT-2 transendothelial migration (Figure 3G) in the absence of cytostatic effects (data not shown). These data demonstrate that the Cx43-mediated GJIC facilitates the invasive behavior of AT-2 cells. Concomitantly, relatively low TEI and high C_i and EPI were observed for AT-2_Fi3 cells. The lack of correlation between Cx43 expression and transmembrane migration index observed also for AT-2_Ep3 and AT-2_Fi1 cells (Figure 3A and B; cf. Figure 3F) suggests a role for cell elasticity and motility in the determination of AT-2 transmigration efficiency. Considerable TEI and EPI values estimated for AT-2_Ep3 cells indicate that these cells may participate in the formation of the invasive Cx43^{bright} AT-2 subset together with AT-2_Fi2-like cells (see Figure 1). These observations show that functional Cx43 is necessary but not sufficient for high invasiveness of Snail-1^{bright}/Cx43^{bright} AT-2 cells. A set of properties characteristic of post-EMT cells, i.e. permissive elasticity and high motile activity, plays the primary role in AT-2 transmigration.

Reciprocal links between Snail-1 signaling and Cx43 determine the invasive potential of prostate cancer cells

The postulated role of mutual interrelations between elasticity, motility and Cx43 expression in determining AT-2 invasive potential prompted us to examine Snail-1 involvement in the regulation of AT-2 invasiveness and Cx43 expression. TGF-β treatment resulted in Snail-1 and Cx43 upregulation in AT-2_Ep1 cells, evoked their EMT and increased transmigration potential and motile activity (Figure 4A; see Supplementary Figure S4A, available at *Carcinogenesis* Online for the data on AT-2_Ep2 and AT-2_Ep3 cells). Corresponding phenotypic shifts were observed in AT-2_Ep1 cells upon ectopic overexpression of Snail-1 (Figure 4B). EMT and Cx43 upregulation was also seen in epithelioid human prostate cancer DU-145 cells upon TGF-β treatment (Supplementary Figure S4B, available at *Carcinogenesis* Online) and ectopic Snail-1 overexpression (Figure 4C). In contrast, downregulation of Cx43 accompanied Snail-1 induction and EMT in TGF-β-treated PNT-2 cells (Supplementary Figure S4C, available at *Carcinogenesis* Online). These observations confirm the sensitivity of AT-2 cells to EMT-promoting signals and suggest that functional links exist between Snail-1 and Cx43 in prostate cancer cells. Accordingly, increased Snail-1 and Cx43 expression levels were observed in TGF-β–treated, invasive AT-2_Fi2 cells (Figure 5A). In contrast, transient Snail-1 silencing in AT-2_Fi2 cells resulted in the inhibition of Cx43 expression and slightly delayed mesenchymal–epithelial transition-related reactions of AT-2_Fi2 cells, including morphological changes, attenuated transendothelial migration and reduced cell elasticity and motility (Figure 5B). Slight Cx43 upregulation was also observed upon TGF-β treatment in MAT-LyLu cells (Figure 5C). Cx43 downregulation, evoked by Snail-1 silencing, was accompanied by the attenuation of MAT-LyLu (Figure 5D) and DU-145 invasiveness (Supplementary Figure S5, available at *Carcinogenesis* Online), which confirms that Snail-1 is a functional linker between the invasive phenotype of prostate cancer cells and Cx43 expression.

Finally, the existence of feedback loops between Cx43 and Snail-1 was indicated by Cx43 silencing experiments. Transient Snail-1 downregulation upon Cx43 silencing in AT-2_Fi2 cells was followed by the inhibition of their transendothelial migration, cellular stiffening (Figure 6A), phenotypic shifts toward epithelioid morphology and the inhibition of cell motility (Figure 6B). Immunoblotting and tandem mass spectrometry of Cx43 coimmunoprecipitates revealed no interaction between Cx43 and Snail-1 in AT-2_Fi2 and AT-2_Ep1 cells (Figure 6C). Instead, α- and β-tubulin were bound to Cx43 in AT-2_Fi2 and, to a lesser degree, in AT-2_Ep1 cells (see Supplementary Table S1, available at *Carcinogenesis* Online). Heterogeneity of 'detergent-insoluble' Snail-1/Cx43 staining in AT-2_Fi2 subclones (Supplementary Figure S2, available at *Carcinogenesis* Online) indicates that 'secular' shifts may also govern the interaction between Cx43 and microtubules and participate in AT-2 diversity. Accordingly, FRET analyses demonstrated increased basic levels of Cx43/α-tubulin interaction in AT-2_Fi2 in comparison with AT-2_Ep1 cells and the induction of this interaction in AT-2_Ep1 cells in response to TGF-β (Figure 6D). They correlated with relatively high basic nuclear p-Smad2 levels seen in AT-2_Fi2 compared with AT-2_Ep1 cells and with an induction of nuclear translocation of p-Smad2 in TGF-β-treated AT-2_Ep1 cells (Figure 6E, see Supplementary Figure S6, available at *Carcinogenesis* Online). These correlative data indicate that interactions between Cx43 and microtubules may delimit the involvement of Cx43 in the signaling loops that determine the basic invasive phenotype of prostate cancer cells.

Discussion

The function of Cx43 in the development of versatile cancers, including prostate cancer, was investigated using a number of *in vivo* and *in vitro* models (15,19,20,40). Histological and genetic engineering strategies have predominantly been employed to discriminate between

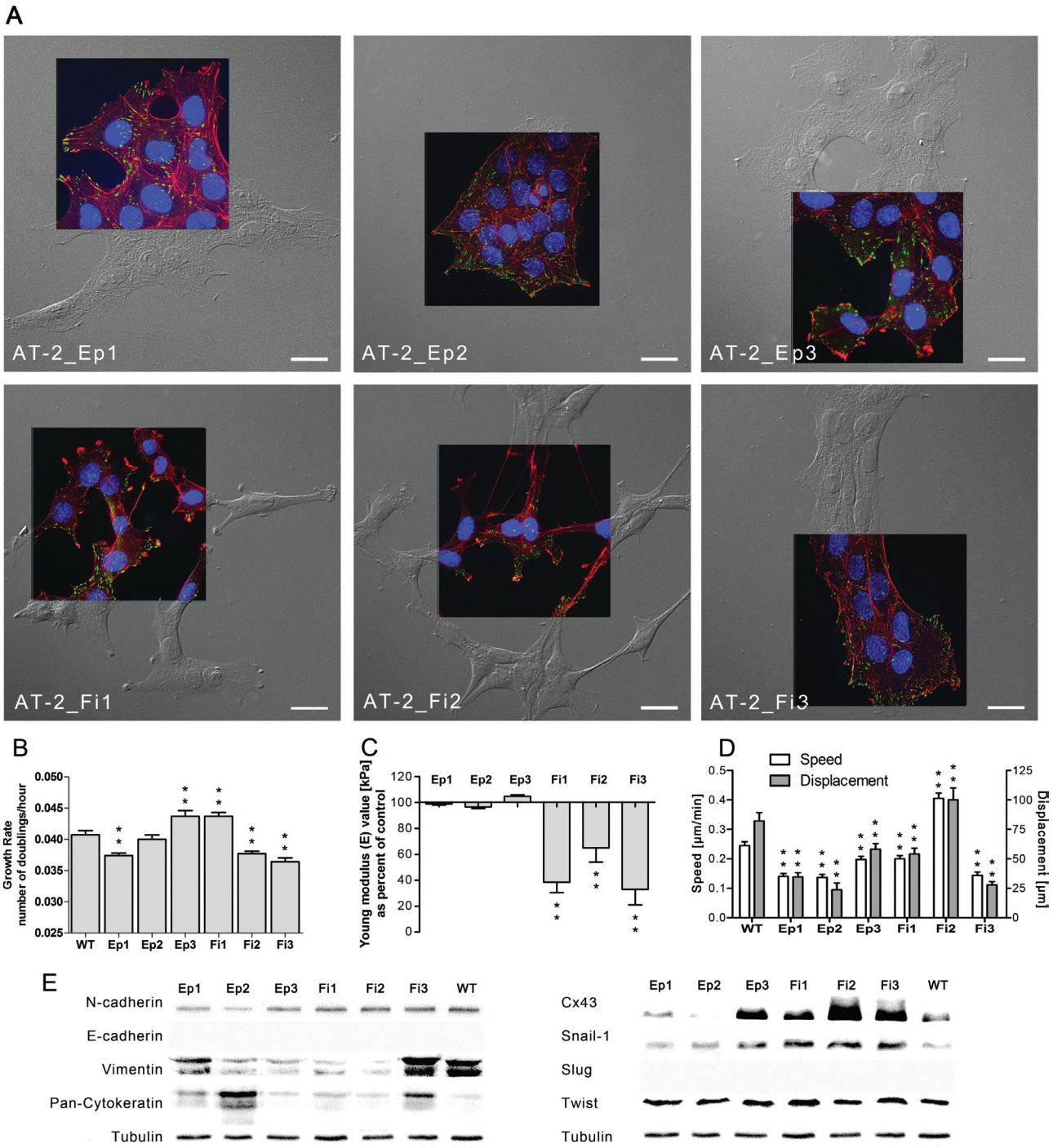

Fig. 2. Phenotypic heterogeneity of AT-2 subclones. (**A**) AT-2 subclones were seeded at the density of 50 cells/cm^2, cultivated for 72 h, fixed/permeabilized with FA/Triton X-100 and stained against vinculin (green) and F-actin (red). Morphology and actin cytoskeleton architecture (inserts) of the cells forming epithelioid (AT-2_Ep1—AT-2_Ep3) and fibroblastoid clones (AT-2_Fi1—AT-2_Fi3) were visualized with Nomarski interference contrast and total internal reflection fluorescence microscopy, respectively. Scale bar: 25 µm. (**B**) Growth rates of AT-2 subclones. Cells were seeded (10^4 cells/cm^2), counted every 24 h for 5 days and population doubling times were calculated from growth curves. Error bars represent SEM. $^{**}P < 0.01$ (t-student's test) versus wt cells. (**C**) AT-2 subclones were seeded at the density of 2×10^2 cells/cm^2, and their nanomechanical elasticity probed with AFM (see Figure 1D and Supplementary Figure S1A, available at *Carcinogenesis* Online). Averaged E values are expressed as a percent of control (AT-2 wt). Error bars represent SEM. $^{**}P < 0.01$ (Student's *t*-test). (**D**) Averaged movement parameters of AT-2 subclones seeded at the density of 5×10^4 cells/cm^2 and analyzed with time-lapse videomicroscopy after 24 h for 8 h. Error bars represent SEM. $^{**}P \leq 0.01$ (Mann-Whitney test). (**E**) Immunoblot analyses of EMT markers (left panel), transcription factors and Cx43 (right panel) in AT-2 subclones were performed as described in Materials and methods. Multiple bands refer to multiple protein isoforms (cytokeratins and vimentin). All results are representative of three independent experiments.

GJIC-dependent and GJIC-independent mechanisms of Cx43 involvement in cancer progression. These studies demonstrated the predilection of Cx43-positive cells for local invasion in a range of cancers (9,20). However, histological approaches mainly provide descriptive snapshots at the points of tissue harvest, whereas phenotypic uniformity of cells is necessary for reliable interpretation of 'gain-of-function' data. Therefore, neither of these approaches was sufficient to model the dynamics of intratumoral heterogeneity. Our study filled this gap

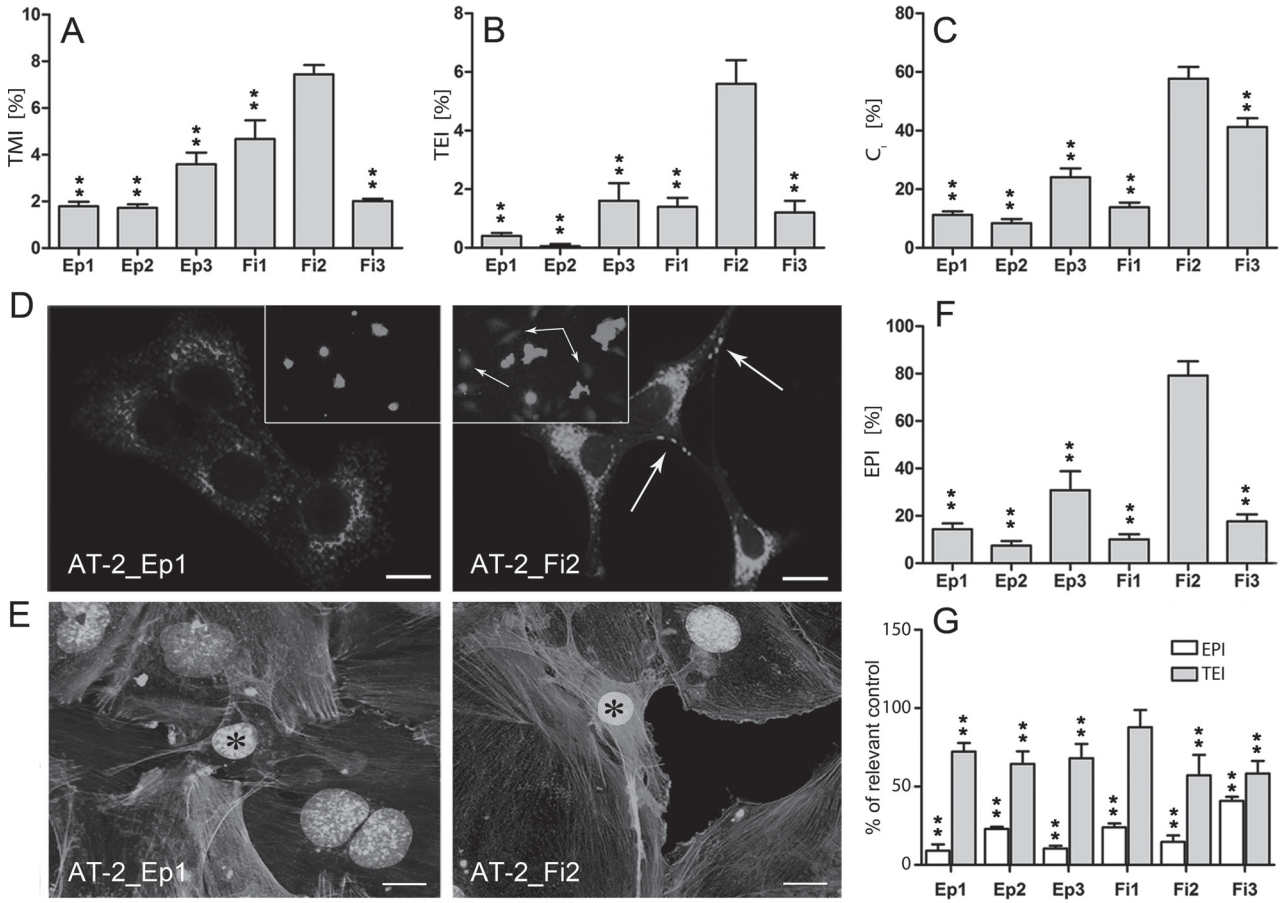

Fig. 3. Cx43-mediated GJIC is involved in the transendothelial migration of AT-2 cells. (**A**) AT-2 cells (3×10^4/cm^2) were seeded onto microporous membranes, allowed to transmigrate for 24–144 h and transmembrane migration index (expressed as % of seeded cells) was estimated. (**B**) AT-2 cells (5×10^3 cells/cm^2) were seeded onto microporous membranes covered with confluent monolayers of HMEC cells and TEI was calculated as in A. (**C**) AT-2 cells were loaded with calcein (see Materials and methods) and seeded onto confluent HMEC monolayers. GJIC between AT-2 and endothelial cells is expressed as coupling index (C_i; $N = 200$). (**D**) MetOH/Acetone-fixed AT-2_Fi2 and AT-2_Ep1 cells were stained against Cx43 and Cx43-positive plaques (arrows) were visualized as described in Materials and methods. Inserts show calcein transfer between AT-2 and HMEC (arrow; see C). Scale bar: 25 µm. (**E**) AT-2 cells were seeded (5×10^3 cells/cm^2) on HMEC monolayer, cultivated for 6 h, fixed/permeabilized with FA/Triton X-100 and stained against F-actin and DNA (marked with *). (**F**) Cells were prepared as in E and the EPI of AT-2 subclones were calculated (see Materials and methods) (**G**) 18-alpha-glycyrrhetinic acid-pre-treated (50 µM; 6 h) AT-2 cells were prepared as in E. TEI and EPI values were calculated as in B and F, respectively. Error bars represent SEM. $^{**}P \le 0.01$ (Student's *t*-test) versus AT-2_Fi2 (A, B, C and F) or versus 18-alpha-glycyrrhetinic acid-untreated cells (**G**). All results are representative of three independent experiments.

because we managed to show the complexity of Cx43 functions in a cellular system that spontaneously recapitulated the events crucial for clonal evolution of invasive cancer cells.

Differences in expression of EMT markers, morphology, motility and growth rates between phenotypically stable, morphologically divergent AT-2 subclones confirm functional heterogeneity of the AT-2 cell line (31). Similar to *in vivo* systems, fast-cycling, 'secular' transitions participate in the maintenance of the basic steady-state of cancer cell heterogeneity *in vitro* (41). On the other hand, the persistence of a cellular invasive phenotype through multiple cell division cycles is mandatory for cancer invasion (22). Phenotypic stability of AT-2 subpopulations indicates that continual stochastic shifts are responsible for phenotypic heterogeneity and differential invasiveness of single AT-2 cells. Noteworthy, the sources of phenotypic heterogeneity of primary tumors and of evolutionary divergence between metastatic outgrowths differ considerably from those responsible for cell line heterogeneities (42). These differences result from the complexity of environmental cues to which cancer cells are exposed *in vivo* (1,43). *In vitro*, clonal selection takes place due to genetic and epigenetic drift over passages and to the differences in proliferation capacity of individual subclones. If not compensated by heritable shifts that continually renew population heterogeneity, this should inevitably lead to a homogeneous population. The phenotypic steadiness of AT-2 cells is indicative of a departure from this scenario, similar to other cellular systems *in vitro* (27,29,30,44–46), including prostate cancer cells (18,47). The existence of invasive Cx43^{bright} subpopulations within this relatively nontumorigenic cell line suggests that it provides an excellent resource for single-cell-based analyses of Cx43 function in prostate cancer progression (48).

The potential of the AT-2 system for modeling the *in vivo* clonal expansion of invasive prostate cancer cells was illustrated by characteristics of AT-2 subsets preselected under conditions mimicking early cancer invasion. These characteristics indicated the predilection of Snail-1^{high}/Cx43^{high} AT-2 cells for a 'cooperative' pattern of migration and invasion. The involvement of cooperative migration has been described for the progression of a variety of tumors, including colorectal and breast tumors (49). Tracing the continual evolution of AT-2 subpopulations that displayed heritable phenotypes provided insight into the mechanisms of cellular heterogeneity within the routinely propagated AT-2 cell line. Efficiency of cell locomotion and, to a lesser degree, elasticity determines the invasive behavior of AT-2 cells. Comparative analyses of the effects of Snail-1 overexpression, Snail-1 silencing and TGF-β on the phenotype of prostate cancer cells indicate that these traits remain under the control of Snail-1. Our data are in agreement with reports on Snail-1 involvement in the regulation of cell properties that determine migratory strategies employed by cancer cells (24,50). Because TGF-β is involved in paracrine loops

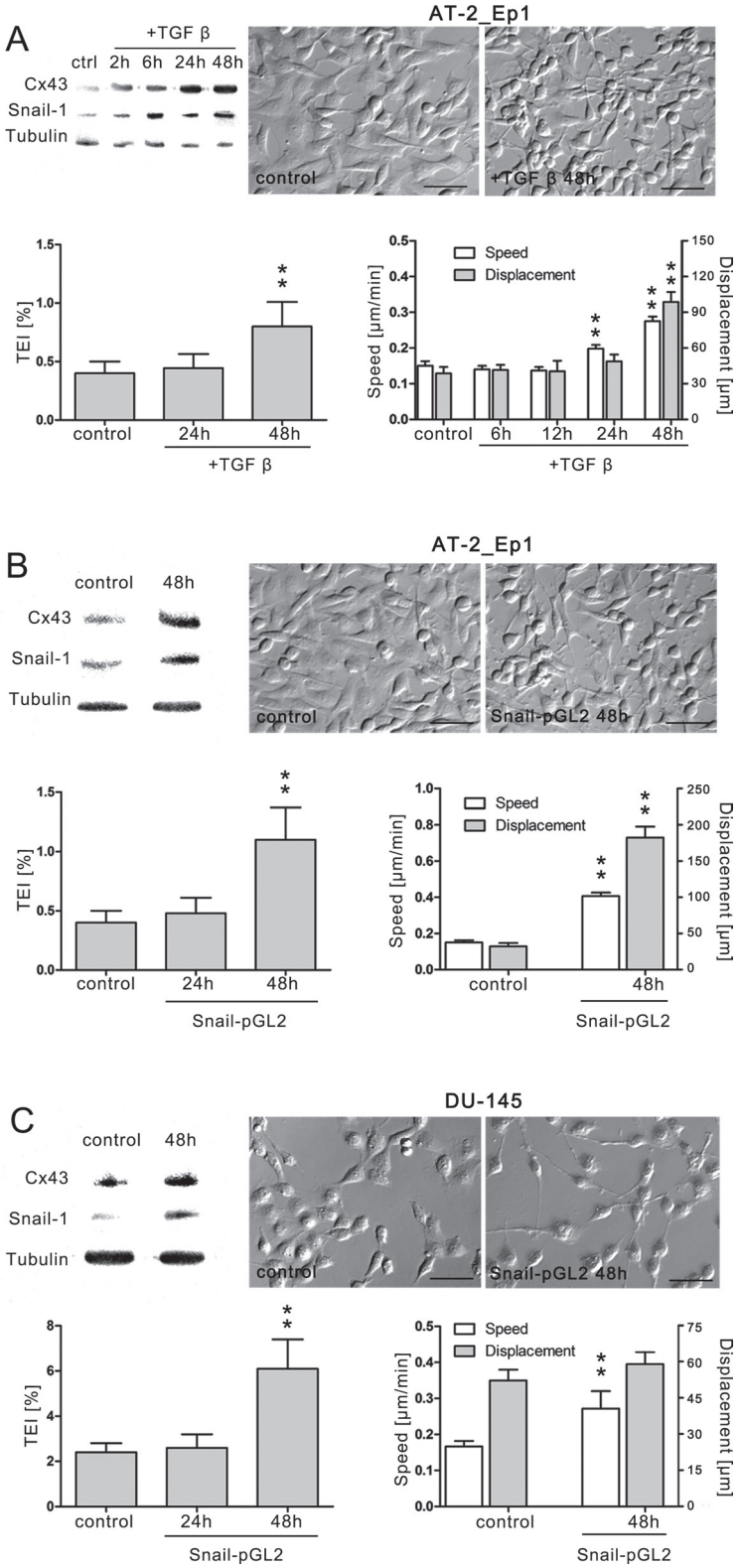

Fig. 4. Activation of Snail-1 signaling evokes EMT and increases Cx43 expression in epithelioid prostate cancer cells. (**A**) AT-2_Ep1 cells were treated with TGF-β (10 ng/ml) 24 h after seeding. Snail-1/Cx43 expression levels (upper left), cell morphology (upper right), TEI (lower left; expressed as % of seeded cells) and motility (lower right; registered for 8 h) were analyzed with immunoblotting, IMC microscopy, transmigration tests and time-lapse videomicroscopy, respectively, at the indicated timepoints and compared with untreated control (see Material and methods, Figures 1 and 3). Error bars represent SEM. Statistical significance tested by the non-parametric Mann–Whitney (motility) and Student's *t*-test (TEI; $^{**}P \leq 0.01$). Scale bar: 50 μm. (**B**) AT-2_Ep1 cells were transfected with Snail_pGL2 plasmid. Cx43 expression (upper left), morphology (upper right), TEI (lower left) and motility (lower right) were analyzed at indicated timepoints after plasmid administration and compared with control as in A. No effects of empty plasmid on cell parameters were observed throughout the experiments. (**C**) Cx43 expression (upper left), morphology (upper right), TEI (lower left) and motility (lower right) were analyzed in Snail_pGL2-transfected DU-145 cells as in B. All results are representative of three independent experiments.

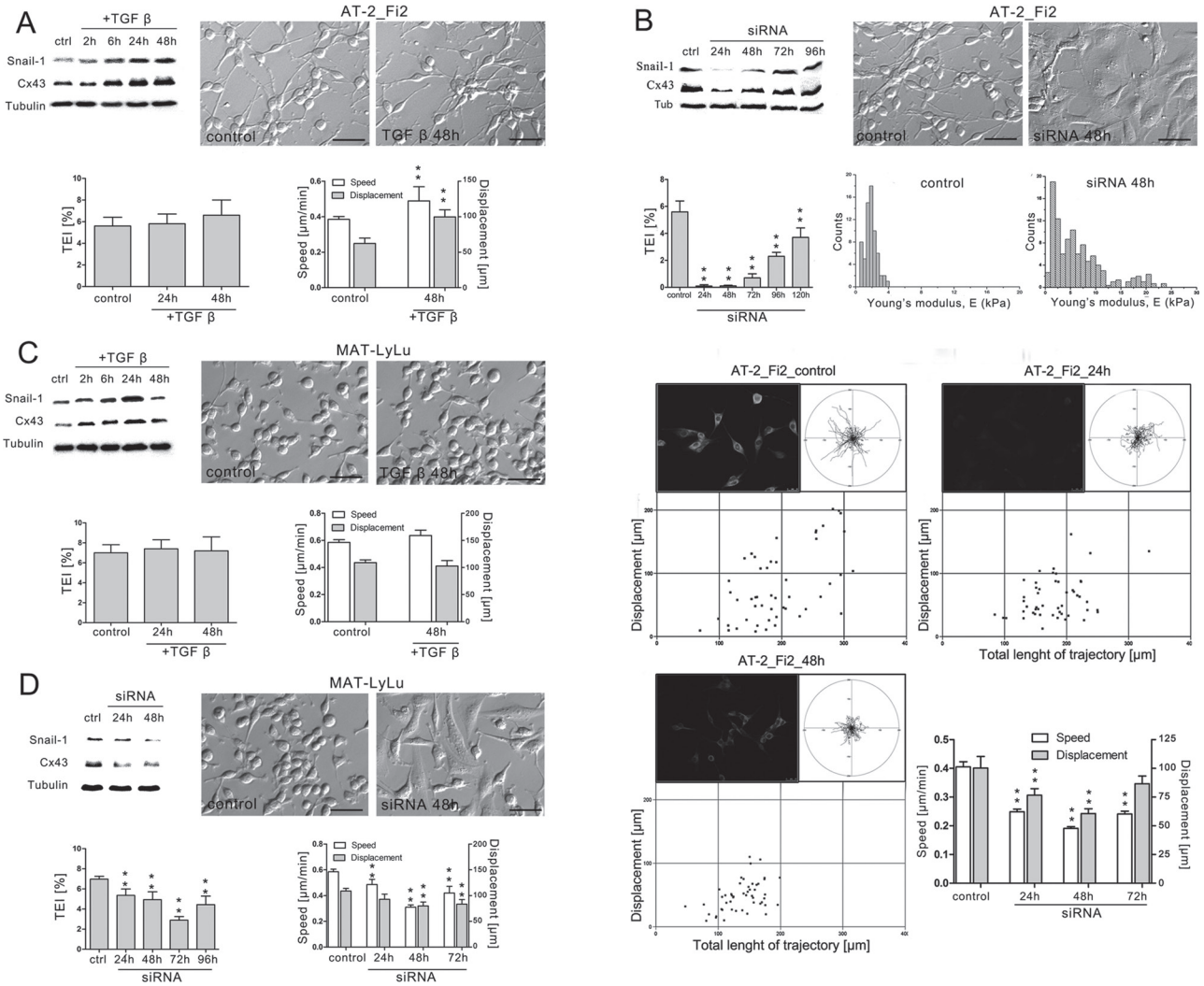

Fig. 5. Snail-1 signaling determines fibroblastoid phenotype of AT-2_Fi2 and MAT-LyLu cells. (**A**) AT-2_Fi2 cells were treated with TGF-β (10 ng/ml) 24 h after seeding. Snail-1/Cx43 expression levels (upper left), cell morphology (upper right), TEI (lower left; expressed as % of seeded cells) and motility (lower right; registered for 8 h) were analyzed with immunoblotting, IMC microscopy, transmigration tests and time-lapse videomicroscopy, respectively, at the indicated timepoints and compared with untreated control (see Material and methods, Figures 1 and 3). Scale bar: 50 µm. (**B**) Snail-1 expression in AT-2_Fi2 cells was transiently silenced by SNAI-1 siRNA as described in Materials and methods and Cx43 expression levels were estimated at the indicated timepoints with immunoblotting (upper left). Cell morphology (upper right) was visualized with IMC. TEI (expressed as % of seeded cells; middle left) was estimated by transmigration tests at the indicated timepoints (see Material and methods). Error bars represent SEM. $^{**}P \leq 0.01$ (Student's *t*-test). Nanomechanical elasticity of AT-2_Fi2 cells was probed with AFM (middle right, see Material and methods and Figure 1). E values represent Young's modulus given in kilopascals (kPa). Motility of AT-2_Fi2 cells (lower panel) was analyzed by time-lapse videomicroscopy. Dot-plots and column chart show movement parameters at the indicated time points. Cell trajectories are depicted as circular diagrams (axis scale in micrometer) drawn with the initial point of each trajectory placed at the origin of the plot (registered for 8 h; $N > 50$). Statistical significance was performed with the non-parametric Mann–Whitney test ($^{**}P \leq 0.01$ versus control). Error bars represent SEM. Inserts depict Cx43 expression visualized by immunostaining of MetOH/Ac fixed, siRNA silenced cells. No effects of empty siRNA-A on cell parameters were observed throughout the experiments. (**C**) MAT-LyLu cells were treated with TGF-β (10 ng/ml) and analyzed as in A. (**D**) Cx43 expression (upper left), morphology (upper right), TEI (lower left) and motility (lower right) of MAT-LyLu cells undergone Snail-1 silencing were analyzed as in A. All results are representative of three independent experiments.

that boost the invasive behavior of cancer cells (50–52), these observations also link the proinvasive cell phenotype to communication networks between cells and their microenvironment.

We also showed subtle differences in Snail-1 and EMT-related protein expression patterns in genetically untouched and non-stimulated AT-2 subclones. Shifts in the abundance of Snail-1^{bright}, Snail-1^{dim} and Snail-1^{low} populations, paralleled by a similar pattern of Snail-1 expression heterogeneity, were observed in AT-2 subclones. Together with the quality of phenotypic shifts evoked in AT-2, DU-145 and MAT-LyLu cells by ectopic changes of Snail-1 expression, they indicate that Snail-1 participated in 'incomplete' transitions between epithelioid and fibroblastoid phenotypes of AT-2 cells. 'Incomplete' EMT-related transitions have long been suggested to participate in the heterogeneity of malignant carcinoma cell invasiveness. There are numerous examples of advanced carcinomas that adopt some mesenchymal features yet retain characteristics of well-differentiated epithelial cells (40,53–55). It is premature to conclude on the mechanisms underlying the divergence of the Snail-1 expression pattern within AT-2 subpopulations. However, subtle differences in cell susceptibility to Snail-1 oscillations may account for different patterns of 'secular' and persistent reprogramming of AT-2 cells (23), for heritable phenotypic divergence of AT-2 cells and their differential tendency for invasion. The heterogeneous pattern of detergent-insoluble Snail-1/Cx43 staining in AT-2 subclones may indirectly confirm this notion. On the other hand, the correlation between Cx43 and Snail-1 expressions observed in AT-2 subsets at the population and

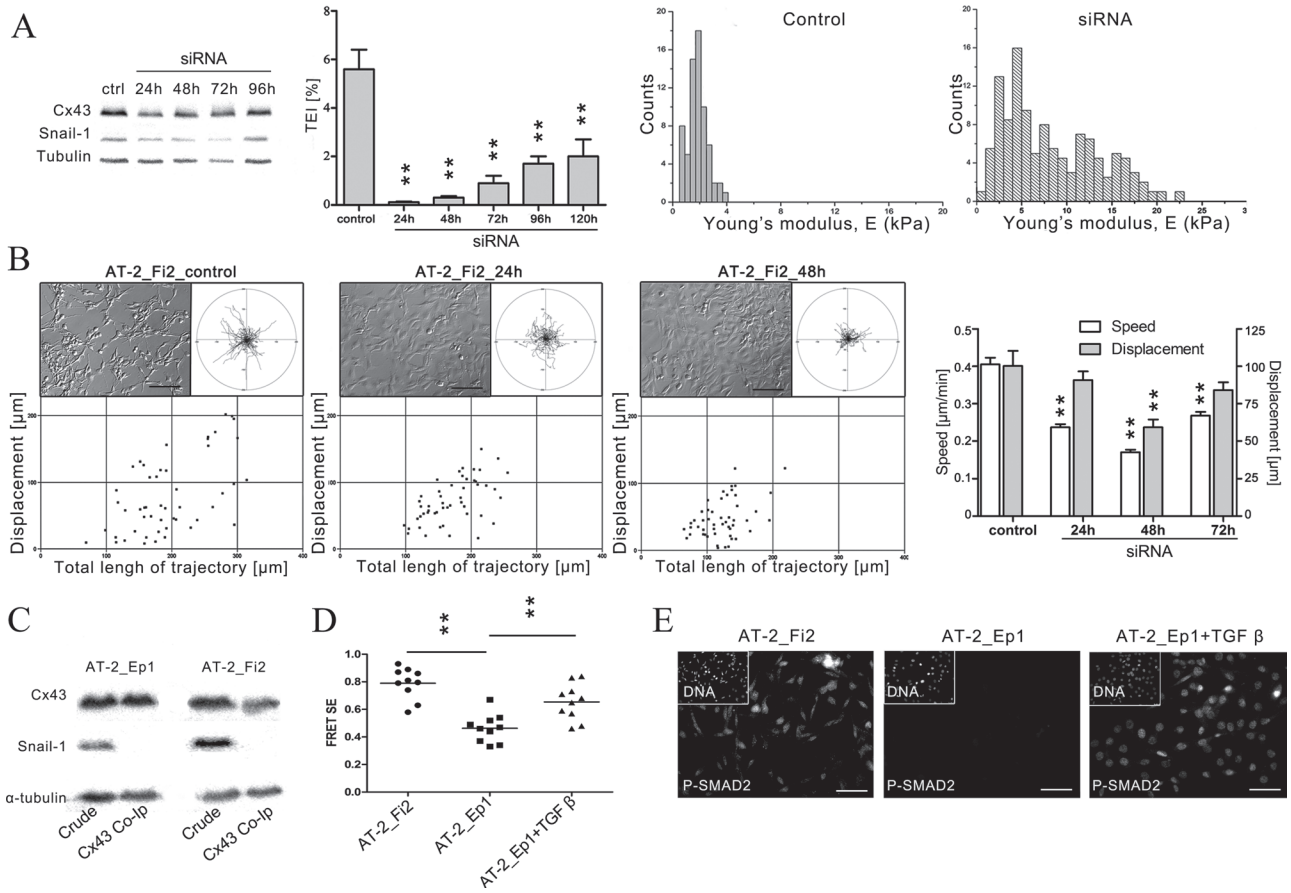

Fig. 6. Feedback loops between Snail-1 signaling and Cx43 in AT-2 cells. (**A**) Cx43 expression was transiently silenced in AT-2_Fi2 cells by esiRNA GJA1 as described in Materials and methods and Snail-1 expression levels were estimated at the indicated timepoints with immunoblotting (left panel). TEI (expressed as % of seeded cells; middle left) was estimated by transmigration tests at the indicated timepoints (see Figure 5B). Error bars represent SEM. $^{**}P \leq 0.01$ (Student's *t*-test). Nanomechanical elasticity of AT-2_Fi2 cells was probed after 48 h with AFM (right, see Figure 5B). E values represent Young's modulus given in kilopascals (kPa). (**B**) Motility of AT-2_Fi2 cells was estimated by time-lapse videomicroscopy (see Figure 5B). Statistical significance tested by the non-parametric Mann–Whitney test ($^{**}P \leq 0.01$). Inserts depict cell morphology visualized by IMC. Scale bar: 50 µm. No effects of empty siRNA-A on cell parameters were observed throughout the experiments. (**C**) Clarified lysates from AT-2_Fi2 and AT-2_Ep1 cells were subjected to immunoprecipitation with anti-Cx43 antibody and then analyzed by immunoblotting with the indicated antibodies. (**D**) pmTurquoise2-α-Tubulin and eYFP-Cx43 was expressed in AT-2_Fi2 and AT-2_Ep1 cells, and FRET SE was estimated after 48 h. TGF-β (10 ng/ml) was added to AT-2_Ep1 cells 30 min. before the measurement. Each point represents an averaged single cell measurement from the region of interest indicated in Supplementary Figure S6, available at *Carcinogenesis* Online. $^{**}P \leq 0.05$ (Student's *t*-test). (**E**) AT-2_Fi2 (left), AT-2_Ep1 (control, middle) and TGF-β-treated AT-2_Ep1 cells (10 ng/ml; 30 min; right) were fixed/permeabilized with FA/Triton X-100 and stained against p-Smad2. Scale bar: 25 µm. All results are representative of three independent experiments.

single cell levels enabled a first inspection of the complexity of the links between cancer cell invasiveness and Cx43 functions. A similar correlation was seen in MAT-LyLu and DU-145 cells subjected to TGF-β treatment, Snail-1 overexpression and silencing, but not in TGF-β-treated normal PNT-2 cells. These observations explain why highly motile and elastic prostate cancer cells express elevated Cx43 levels.

We propose two mechanisms that could favor invasion of $Cx43^{bright}$ AT-2 cells. Because of the correlation between Cx43 and Snail-1 expressions and the role of Snail-1 in determination of the invasive cell phenotype, high Cx43 levels may accompany AT-2 predilection for invasive behavior. GJIC-dependent selective pressure on the recruitment of $Cx43^{bright}$ cells into the AT-2 invasive front was illustrated by preferential transmigration of AT-2_Fi2 cells through endothelial layers, high levels of detergent-insoluble Cx43 and inhibition of AT-2_Fi2 transendothelial migration by the GJIC blocker. Thus, Cx43 can facilitate cancer invasion by mediating GJIC between cancer and endothelial cells during intra- and extravasation downstream of cell motility and elasticity (9,20). On the other hand, shifts toward the non-invasive phenotype were evoked by Cx43 silencing in AT-2_Fi2 cells. This finding indicates that Cx43 determines invasive AT-2 behavior in a GJIC-independent manner. Intracellular Cx43 and unpaired connexons have been shown to regulate the cell cycle, conduit intercellular signaling, participate in cell adhesion and directed migration via interactions with the gap junction proteome (25,56–59) and affect the secretome of prostate cancer cells (19). Cx43 may thus favor prostate cancer cell invasion through divergent effects on cell motility (60). Differences in the intensity of Cx43/α-tubulin interactions and p-Smad2 localization in AT-2_Fi2 and AT-2_Ep1 cells suggest that microtubule-bound Cx43 fraction participates in the feedback loops between Cx43 and Snail-1 crucial for the phenotypic diversity of AT-2 cells (33). Different cellular sensitivity to GJIC-independent signals from Cx43 may additionally account for the phenotypic divergence of AT-2 subclones. More elaborate studies are underway to explore these interrelations.

Our study shows the complexity of Cx43 functions during the metastatic cascade of prostate cancer and offers an explanation of how Cx43 can confer a selective advantage on the cells during cooperative invasion. Reciprocal links between GJIC-dependent and GJIC-independent Cx43 functions may, at least partly, account for the formation of invasive subsets within the prostate tumor cell mass *in vivo*. Actually, scarce subpopulation(s) of invasive AT-2 cells identified in this study can be responsible for low, but detectable, AT-2

tumorigenicity (48). Thus, the applied AT-2 model is adequate for investigating the Cx43-dependent mechanisms underlying the metastatic behavior of prostate cancer cells. Preselection and expansion of phenotypically distinct cellular subpopulations under conditions imitating different steps of the metastatic cascade helped us to negotiate the barriers and limitations imposed by the phenotypic uniformity of genetically engineered cellular models. When applied to cell populations directly propagated from cancer biopsies, this strategy may open new perspectives for the recapitulation of Cx43 prognostic significance in other cancers characterized by high latency periods.

Supplementary material

Supplementary Table S1 and Figures S1–S6 can be found at http://carcin.oxfordjournals.org/

Funding

Polish National Science Centre (2011/01/B/NZ3/00004 to J.C.); the Faculty of Biochemistry, Biophysics and Biotechnology of the Jagiellonian University is a beneficiary of structural funds from the European Union (UDA-POIG.01.03.01-14-036/09-00, POIG.02.01.00-12-064/08, POIG.01.02-00-109/09, POIG.02.01.00-12-167/08).

Acknowledgements

We wish to thank Małgorzata Pierzchalska for the coimunoprecipitation tutorial and Halina Gabryś for critically reviewing the manuscript.

Conflict of Interest Statement: None declared.

References

1. Sottoriva,A. *et al*. (2010) Exploring cancer stem cell niche directed tumor growth. *Cell Cycle*, **9**, 1472–1479.
2. Langley,R.R. *et al*. (2011) The seed and soil hypothesis revisited–the role of tumor-stroma interactions in metastasis to different organs. *Int. J. Cancer*, **128**, 2527–2535.
3. Friedl,P. *et al*. (2011) Cancer invasion and the microenvironment: plasticity and reciprocity. *Cell*, **147**, 992–1009.
4. Jerónimo,C. *et al*. (2011) Epigenetics in prostate cancer: biologic and clinical relevance. *Eur. Urol*., **60**, 753–766.
5. Shibata,M. *et al*. (2013) The roots of cancer: stem cells and the basis for tumor heterogeneity. *Bioessays*, **35**, 253–260.
6. Leithe,E. *et al*. (2006) Downregulation of gap junctions in cancer cells. *Crit. Rev. Oncog*., **12**, 225–256.
7. Mol,A.J. *et al*. (2007) New experimental markers for early detection of high-risk prostate cancer: role of cell-cell adhesion and cell migration. *J. Cancer Res. Clin. Oncol*., **133**, 687–695.
8. Kumar,S. *et al*. (2009) Mechanics, malignancy, and metastasis: the force journey of a tumor cell. *Cancer Metastasis Rev*., **28**, 113–127.
9. Naus,C.C. *et al*. (2010) Implications and challenges of connexin connections to cancer. *Nat. Rev. Cancer*, **10**, 435–441.
10. Lin,J.H. *et al*. (2002) Connexin 43 enhances the adhesivity and mediates the invasion of malignant glioma cells. *J. Neurosci*., **22**, 4302–4311.
11. Elzarrad,M.K. *et al*. (2008) Connexin-43 upregulation in micrometastases and tumor vasculature and its role in tumor cell attachment to pulmonary endothelium. *BMC Med*., **6**, 20.
12. Ito,A. *et al*. (2000) A role for heterologous gap junctions between melanoma and endothelial cells in metastasis. *J. Clin. Invest*., **105**, 1189–1197.
13. Zhang,W. *et al*. (2003) Communication between malignant glioma cells and vascular endothelial cells through gap junctions. *J. Neurosurg*., **98**, 846–853.
14. Pollmann,M.A. *et al*. (2005) Connexin 43 mediated gap junctional communication enhances breast tumor cell diapedesis in culture. *Breast Cancer Res*., **7**, R522–R534.
15. Kanczuga-Koda,L. *et al*. (2006) Increased expression of connexins 26 and 43 in lymph node metastases of breast cancer. *J. Clin. Pathol*., **59**, 429–433.
16. Naoi,Y. *et al*. (2007) Connexin26 expression is associated with lymphatic vessel invasion and poor prognosis in human breast cancer. *Breast Cancer Res. Treat*., **106**, 11–17.
17. Miekus,K. *et al*. (2005) Contact stimulation of prostate cancer cell migration: the role of gap junctional coupling and migration stimulated by heterotypic cell-to-cell contacts in determination of the metastatic phenotype of Dunning rat prostate cancer cells. *Biol. Cell*, **97**, 893–903.
18. Szpak,K. *et al*. (2011) DU-145 prostate carcinoma cells that selectively transmigrate narrow obstacles express elevated levels of Cx43. *Cell. Mol. Biol. Lett*., **16**, 625–637.
19. Lamiche,C. *et al*. (2012) The gap junction protein Cx43 is involved in the bone-targeted metastatic behaviour of human prostate cancer cells. *Clin. Exp. Metastasis*, **29**, 111–122.
20. Czyż,J. *et al*. (2012) The role of connexins in prostate cancer promotion and progression. *Nat. Rev. Urol*., **9**, 274–282.
21. Nauseef,J.T. *et al*. (2011) Epithelial-to-mesenchymal transition in prostate cancer: paradigm or puzzle? *Nat. Rev. Urol*., **8**, 428–439.
22. Geiger,T.R. *et al*. (2009) Metastasis mechanisms. *Biochim. Biophys. Acta*, **1796**, 293–308.
23. Graf,T. *et al*. (2008) Heterogeneity of embryonic and adult stem cells. *Cell Stem Cell*, **3**, 480–483.
24. Savagner,P. (2010) The epithelial-mesenchymal transition (EMT) phenomenon. *Ann. Oncol*., **21** (suppl. 7), vii89–vii92.
25. Mroue,R.M. *et al*. (2011) Connexins and the gap in context. *Integr. Biol. (Camb)*., **3**, 255–266.
26. Cichocki,F. *et al*. (2013) Epigenetic regulation of NK cell differentiation and effector functions. *Front. Immunol*., **4**, 55.
27. Langley,R.R. *et al*. (2007) Tumor cell-organ microenvironment interactions in the pathogenesis of cancer metastasis. *Endocr. Rev*., **28**, 297–321.
28. Tchou-Wong,K.M. *et al*. (2006) Rapid chemokinetic movement and the invasive potential of lung cancer cells; a functional molecular study. *BMC Cancer*, **6**, 151.
29. Wysoczynski,M. *et al*. (2007) Leukemia inhibitory factor: a newly identified metastatic factor in rhabdomyosarcomas. *Cancer Res*., **67**, 2131–2140.
30. Bechyne,I. *et al*. (2012) Functional heterogeneity of non-small lung adenocarcinoma cell sub-populations. *Cell Biol. Int*., **36**, 99–103.
31. Musialik,E. *et al*. (2013) Morpho-physiological heterogeneity of cells within two rat prostate carcinoma cell lines AT-2 and MAT-LyLu differing in the degree of malignancy observed by cell cloning and the effects of caffeine, theophylline and papaverine upon a proportion of the clones. *Oncol. Rep*., **29**, 1789–1796.
32. Baran,B. *et al*. (2009) Blood monocytes stimulate migration of human pancreatic carcinoma cells *in vitro*: the role of tumour necrosis factor - alpha. *Eur. J. Cell Biol*., **88**, 743–752.
33. Dai,P. *et al*. (2007) Cx43 mediates TGF-beta signaling through competitive Smads binding to microtubules. *Mol. Biol. Cell*, **18**, 2264–2273.
34. Wiśniewski,J.R. *et al*. (2009) Universal sample preparation method for proteome analysis. *Nat. Methods*, **6**, 359–362.
35. Sarna,M. *et al*. (2013) Nanomechanical analysis of pigmented human melanoma cells. *Pigment Cell Melanoma Res*., **26**, 727–730.
36. Wybieralska,E. *et al*. (2011) Fenofibrate attenuates contact-stimulated cell motility and gap junctional coupling in DU-145 human prostate cancer cell populations. *Oncol. Rep*., **26**, 447–453.
37. Fujita,N. *et al*. (2003) MTA3, a Mi-2/NuRD complex subunit, regulates an invasive growth pathway in breast cancer. *Cell*, **113**, 207–219.
38. Smyth,J.W. *et al*. (2010) Limited forward trafficking of connexin 43 reduces cell-cell coupling in stressed human and mouse myocardium. *J. Clin. Invest*., **120**, 266–279.
39. Goedhart,J. *et al*. (2012) Structure-guided evolution of cyan fluorescent proteins towards a quantum yield of 93%. *Nat. Commun*., **3**, 751.
40. Chao,Y. *et al*. (2012) Partial mesenchymal to epithelial reverting transition in breast and prostate cancer metastases. *Cancer Microenviron*., **5**, 19–28.
41. Heppner,G.H. (1984) Tumor heterogeneity. *Cancer Res*., **44**, 2259–2265.
42. Marusyk,A. *et al*. (2010) Tumor heterogeneity: causes and consequences. *Biochim. Biophys. Acta*, **1805**, 105–117.
43. Condeelis,J. *et al*. (2006) Macrophages: obligate partners for tumor cell migration, invasion, and metastasis. *Cell*, **124**, 263–266.
44. Boiko,A.D. *et al*. (2010) Human melanoma-initiating cells express neural crest nerve growth factor receptor CD271. *Nature*, **466**, 133–137.
45. Visvader,J.E. (2011) Cells of origin in cancer. *Nature*, **469**, 314–322.
46. Fredebohm,J. *et al*. (2012) Establishment and characterization of a highly tumourigenic and cancer stem cell enriched pancreatic cancer cell line as a well defined model system. *PLoS One*, **7**, e48503.
47. Zhang,K. *et al*. (2010) PC3 prostate tumor-initiating cells with molecular profile FAM65Bhigh/MFI2low/LEF1low increase tumor angiogenesis. *Mol. Cancer*, **9**, 319.
48. Carter,H.B. *et al*. (1989) Prediction of metastatic potential in an animal model of prostate cancer: flow cytometric quantification of cell surface charge. *J. Urol*., **142**, 1338–1341.

49. Tsuji,T. *et al*. (2009) Epithelial-mesenchymal transition and cell cooperativity in metastasis. *Cancer Res*., **69**, 7135–7139.
50. Katsuno,Y. *et al*. (2013) TGF-β signaling and epithelial-mesenchymal transition in cancer progression. *Curr. Opin. Oncol*., **25**, 76–84.
51. Wesolowska,A. *et al*. (2008) Microglia-derived TGF-beta as an important regulator of glioblastoma invasion–an inhibition of TGF-beta-dependent effects by shRNA against human TGF-beta type II receptor. *Oncogene*, **27**, 918–930.
52. Lang,S.H. *et al*. (2001) Prostate epithelial cell lines form spheroids with evidence of glandular differentiation in three-dimensional Matrigel cultures. *Br. J. Cancer*, **85**, 590–599.
53. Brown,K.A. *et al*. (2004) Induction by transforming growth factor-beta1 of epithelial to mesenchymal transition is a rare event *in vitro*. *Breast Cancer Res*., **6**, R215–R231.
54. Christiansen,J.J. *et al*. (2006) Reassessing epithelial to mesenchymal transition as a prerequisite for carcinoma invasion and metastasis. *Cancer Res*., **66**, 8319–8326.
55. Pinkas,J. *et al*. (2002) MEK1 signaling mediates transformation and metastasis of EpH4 mammary epithelial cells independent of an epithelial to mesenchymal transition. *Cancer Res*., **62**, 4781–4790.
56. Kardami,E. *et al*. (2007) The role of connexins in controlling cell growth and gene expression. *Prog. Biophys. Mol. Biol*., **94**, 245–264.
57. Burra,S. *et al*. (2011) Regulation of cellular function by connexin hemichannels. *Int. J. Biochem. Mol. Biol*., **2**, 119–128.
58. Cotrina,M.L. *et al*. (2008) Adhesive properties of connexin hemichannels. *Glia*, **56**, 1791–1798.
59. Francis,R. *et al*. (2011) Connexin43 modulates cell polarity and directional cell migration by regulating microtubule dynamics. *PLoS One*, **6**, e26379.
60. Tate,A.W. *et al*. (2006) Changes in gap junctional connexin isoforms during prostate cancer progression. *Prostate*, **66**, 19–31.

Received September 4, 2013; revised December 26, 2013; accepted January 17, 2014